PHOTONICS Research

Relative intensity noise in high-speed hybrid square-rectangular lasers

FU-LI WANG, XIU-WEN MA, YONG-ZHEN HUANG,* YUE-DE YANG, JUN-YUAN HAN, AND JIN-LONG XIAO

State Key Laboratory on Integrated Optoelectronics, Institute of Semiconductors & Institute of Material Science and Optoelectronic Technology, University of Chinese Academy of Sciences, Chinese Academy of Sciences, Beijing 100083, China
Corresponding author: yzhuang@semi.ac.cn

Relative intensity noise (RIN) and high-speed modulation characteristics are investigated for an AlGaInAs/InP hybrid square-rectangular laser (HSRL) with square side length, rectangular length, and width of 15, 300, and 2 µm, respectively. Single-mode operation with side-mode suppression larger than 40 dB has been realized for the HSRL over wide variation of the injection currents. In addition, the HSRL exhibits a 3 dB modulation bandwidth of 15.5 GHz, and an RIN nearly approaches standard quantum shot-noise limit $2h\nu/P = -164$ dB/Hz at high bias currents due to the strong mode selection of the square microcavity. With the increase of the DC bias current of the Fabry–Perot section, significantly enhanced modulation bandwidth and decreased RIN are observed. Furthermore, intrinsic parameters such as resonance frequency, damping factor, and modified Schawlow–Townes linewidth are extracted from the noise spectra.   © 2018 Chinese Laser Press

OCIS codes: (140.3948) Microcavity devices; (140.5960) Semiconductor lasers; (270.2500) Fluctuations, relaxations, and noise.

https://doi.org/10.1364/PRJ.6.000193

1. INTRODUCTION

Whispering-gallery mode (WGM) microcavities have attracted increasing attention for potential application as a light source in areas such as optical communication, interconnection, and computing systems for its intrinsic properties such as high-quality factor, small mode volume, low power consumption, and suitability for on-chip integration [1–5]. With increasing demand of high-speed optical communication networks, much effort has been invested into the pursuit of high-speed modulation bandwidth [6–10]. In addition to the modulation speed in characterizing the transmission quality of optical communication links, system noise also plays an important role because it limits the signal-to-noise ratio. Overall noise is contributed by the thermal noise of the optical link, the shot noise of the photodetector, and, most importantly, the relative intensity noise (RIN) of the laser source. The laser RIN is characterized by the relative optical power fluctuation around the steady-state power level, which is related to the optical interference between the coherent laser mode and the spontaneous light emission as well as the laser mode competition [11–13]. A laser with low RIN is essential in the pursuit of high signal fidelity and low bit error rate in optical communication systems, particularly when analog information is transmitted. A Fabry–Perot (FP) diode laser with RIN amplitude of −130 dB/Hz is reported [11]. A tunable sampled-grating distributed Bragg reflector laser with RIN below the photodiode shot noise limit of −160 dB/Hz is

realized [14]. Recently, an oxide vertical-cavity surface-emitting laser achieves a laser RIN almost reaching the standard quantum limit of −154.3 dB/Hz due to the suppression of the mode competition by shrinking the optical modal dimension [15,16]. Recently, a hybrid square-rectangular microlaser (HRSL) with strong mode coupling between WGM and FP mode is proposed and demonstrated for stable single-mode operation with a side-mode suppression ratio (SMSR) larger than 40 dB. Enhanced coupling efficiency to a single-mode fiber is also demonstrated due to the modification effect on the output pattern of the hybrid coupled laser [17,18]. These key merits enable the application of HSRL as a potential light source in optical communication systems and on-chip integrated circuits.

In this paper, we report the direct modulation speed and noise performances of an HSRL. Small signal modulation response and laser RIN characteristics are investigated with the variation of injection current in FP or WGM section while keeping constant of the other one, respectively. A 3 dB bandwidth of 15.5 GHz and a laser RIN almost reaching the standard quantum shot-noise limit are obtained at high bias current. The RIN spectrum shows well-defined peaks at the relaxation oscillation frequency, which is almost in accordance with the resonance peak frequency, as shown in the small signal modulation response curve. Furthermore, inherent parameters such as the resonance frequency, damping factor, and the modified Schawlow–Townes linewidth are extracted from the noise

spectra and compared with that obtained by fitting the small signal modulation curves.

2. STATIC AND DYNAMIC CHARACTERISTICS

A diagram of a hybrid square-rectangular laser is shown in Fig. 1, which consists of an FP cavity with one of the reflection facets replaced by a square-shaped microcavity. The cavity patterns are formed by deep etching passing through the active region, while the output facet can be formed by both etching and cleavage. Lasing resonances are generated by the mode coupling between the WGMs within the square section and FP modes in the rectangular section. An AlGaInAs/InP laser wafer with the active region consisting of eight compressively strained quantum wells is used to fabricate the HSRLs. The detailed process has been described previously as in Refs. [17,18]. A microscope image of a fabricated device is shown in Fig. 1.

After cleaving over the rectangular section to form an output facet, the HSRL is bonded p-side up on an AlN submount with the temperature maintained at 290 K controlled by a thermo-electric cooler. The side length of the square cavity, width, and length of the rectangular cavity are $a = 15$ μm, $d = 2$ μm, and $L = 300$ μm, respectively. The HSRL device is then biased via a 40 GHz microwave picoprobe for the following static, small signal modulation bandwidth, and laser RIN performances measurements. The output power is collected and collimated by a tapered single-mode fiber (SMF). The collected output power versus the FP section current I_{FP} is measured and plotted in Fig. 2(a), for different square biasing currents I_{SQ}. The threshold currents are 21, 10, 8, and 8 mA, and the coupled maximum output powers are 2.01, 2.60, 3.04, and 3.75 mW for $I_{SQ} = 0$, 5, 10, and 15 mA, respectively. The lasing spectrum is plotted in Fig. 2(b) for the HSRL at injection currents of $I_{FP} = 48$ mA and $I_{SQ} = 10$ mA, measured using an optical spectrum analyzer (OSA) at a resolution of 0.02 nm. Single-mode operation is realized at the lasing wavelength of 1542.51 nm with the SMSR of 46 dB. Detailed lasing spectrum in Fig. 2(c) shows evident minor peaks around the main lasing peak, which may be contributed by low Q hybrid modes and affect the small signal modulation curves.

The detailed lasing spectra at different injection currents of I_{FP} and I_{SQ} are further shown in Figs. 3(a) and 3(b). The corresponding dominant mode wavelengths and the SMSRs as

Fig. 2. (a) Output powers coupled into a tapered single-mode fiber versus I_{FP} at fixed I_{SQ} of 0, 5, 10, and 15 mA. (b) Lasing spectrum. (c) Detailed spectrum around dominant lasing mode at $I_{FP} = 48$ mA and $I_{SQ} = 10$ mA showing single-mode operation with an SMSR of 46 dB, for an HSRL with $a = 15$ μm, $d = 2$ μm, and $L = 300$ μm.

functions of I_{FP} and I_{SQ} are shown in Figs. 3(c) and 3(d), marked by hollow circles and solid squares, respectively. With the variation of I_{FP} as $I_{SQ} = 10$ mA, stable single-mode lasing around a wavelength of 1542 nm with SMSRs over 38 dB is obtained for I_{FP} ranging from 10 to 52 mA. In addition, mode hoppings with sharp oscillation of SMSRs are observed as I_{FP} exceeds 52 mA due to mode competition. Dips in SMSRs at 56 and 72 mA are accompanied with mode hopping to adjacent FP modes with shorter wavelengths, while the dip in SMSRs at 62 mA with mode hopping with a wavelength interval of about two times that of the longitudinal mode interval of bare WG mode in the square section is attributed to redshift of the gain spectrum of the square resonator caused by temperature rising with the increase of the injection current.

Fig. 3. Lasing spectra versus different injection currents of (a) I_{FP} as $I_{SQ} = 10$ mA and (b) I_{SQ} as $I_{FP} = 45$ mA. Dominant mode wavelengths and SMSRs as functions of (c) I_{FP} as $I_{SQ} = 10$ mA and (d) I_{SQ} as $I_{FP} = 45$ mA, respectively, for HRSL with $a = 15$ μm, $d = 2$ μm, and $L = 300$ μm.
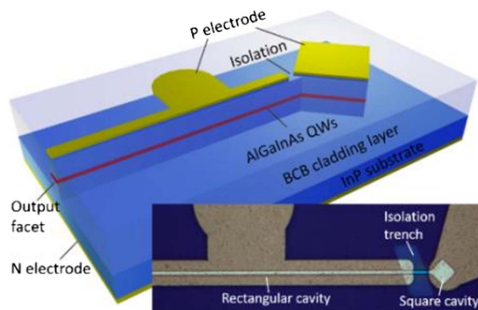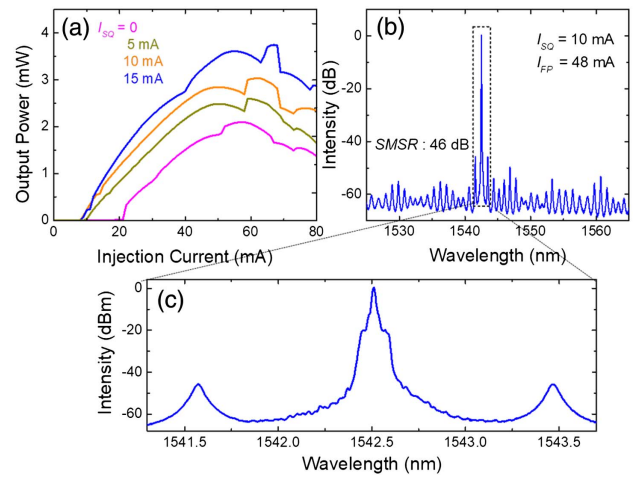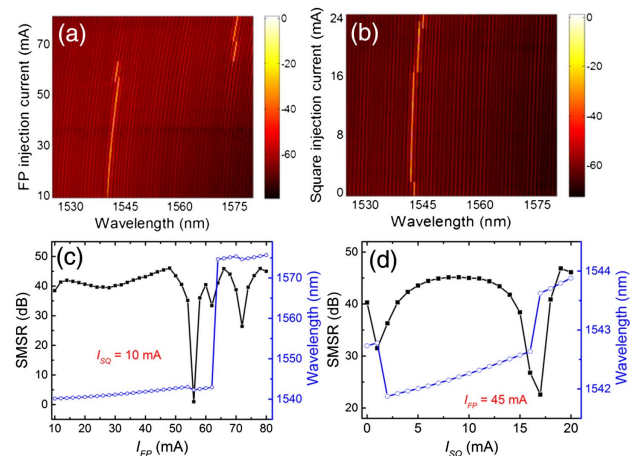

Fig. 1. Schematic and microscopic image of an HSRL with BCB confinement layer. Square and rectangular sections are electrically isolated by a 20 μm isolation trench.

Similarly, the lasing spectra, SMSRs, and the dominant mode wavelengths versus I_{SQ} as $I_{FP} = 45$ mA are measured and illustrated in Figs. 3(b) and 3(d). Single-mode lasing with SMSRs over 40 dB around 1542 nm is obtained, as I_{SQ} increases from 3 to 14 mA. Mode hoppings to adjacent FP modes with dips in SMSRs are also observed. The blueshift of the wavelength around $I_{SQ} = 1$ mA is mainly caused by the free carrier dispersion below the threshold for square section, while the wavelength redshift around $I_{SQ} = 16$ mA is due to the heating effect caused by the increase of injection current.

Furthermore, the hybrid-mode linewidth of the HSRL is measured by using a delayed self-heterodyne detection technique. A 120 m long fiber delay line is used in order to balance the need of eliminating the coherence between the two paths and avoiding the $1/f$ noise effects [19]. And a 200 MHz acousto-optic modulator is used for frequency shifting. The beating signal is obtained after converting into an electrical signal through a 10 GHz bandwidth photodetector. Figure 4 shows the normalized radio frequency (RF) spectrum of the detected beating signal for the lasing mode of the HSRL as $I_{SQ} = 10$ mA and $I_{FP} = 50$ mA, accompanied by Lorentz fit curve shown by the red solid line. The full width at half-maximum of the detected signal is 30 MHz, indicating that the lasing linewidth is 15 MHz.

The small signal modulation response of the HSRL is measured using the schematic shown in Ref. [7]. Small-signal modulation together with the bias current is injected into the FP section through a high-speed microwave picoprobe. The lasing output power is coupled into a tapered fiber and detected by a 50 GHz bandwidth high-speed photodetector. The transferred electrical signals are measured by a network analyzer and illustrated in Fig. 5, with different injection current of I_{FP} and I_{SQ}. As shown in Fig. 5(a), the 3 dB bandwidth increases from 7.3 to 15.1 GHz with corresponding resonance peak decreasing from 5.6 to 3 dB, as I_{FP} increases from 15 to 50 mA and $I_{SQ} = 10$ mA. In contrast, the small signal modulation response curves vary little, as shown in Fig. 5(b) with a 3 dB modulation bandwidth increase from 14 to 15.5 GHz, as I_{SQ} rises from 5 to 15 mA and $I_{FP} = 45$ mA. Minor peaks around 15 GHz are observed in Figs. 5(a) and 5(b), which may be caused by the photon–photon resonance effect [20–22], due to the existence of the minor peaks, as shown in Fig. 2(c).
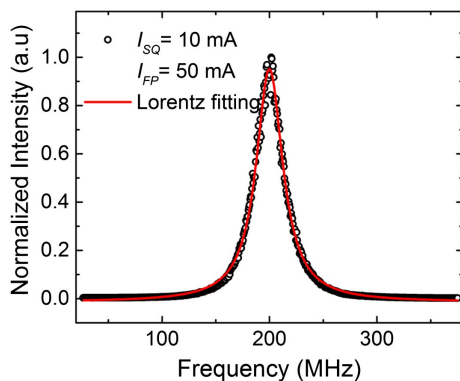

Fig. 4. Normalized RF spectrum of the delayed self-heterodyne interference signal of lasing mode and Lorentzian fit to the measurement data, for the HSRL as $I_{SQ} = 10$ mA and $I_{FP} = 50$ mA.
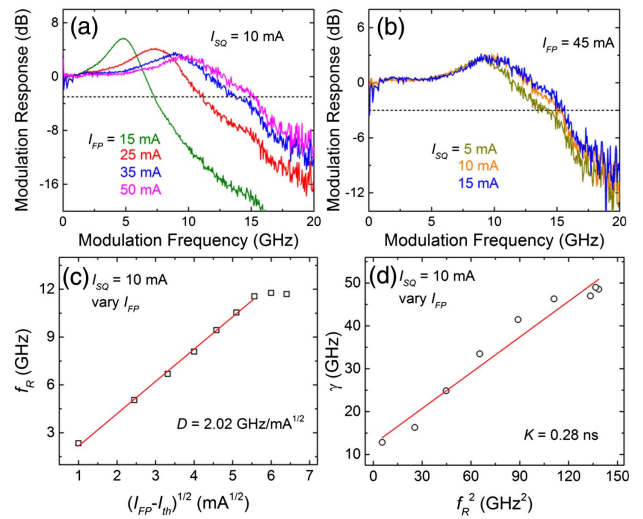

Fig. 5. Small signal modulation responses of the HSRL with $a = 15$ μm, $d = 2$ μm, and $L = 300$ μm at (a) $I_{FP} = 15, 25, 35, 50$ mA and $I_{SQ} = 10$ mA and (b) $I_{SQ} = 5, 10, 15$ mA and $I_{FP} = 45$ mA. (c) Resonance frequency versus square root of the injection current above threshold and (d) corresponding damping factors versus f_R^2 with variation of I_{FP} at $I_{SQ} = 10$ mA.

The measured response curves are fitted by the small signal modulation transfer function [6]. The fitted resonance frequencies f_R versus the square root of the injection current minus the threshold current is shown in Fig. 5(c). A D-factor of 2.02 GHz/mA$^{1/2}$ is obtained considering the linear dependence of the resonance frequency on $(I_{FP} - I_{th})^{1/2}$ [23,24]. The resonance frequency saturates at high bias current due to laser self-heating effect and extrinsic parasitic resistance and capacitance of the devices. Moreover, the damping factor γ as a function of the square of resonance frequency f_R^2 is shown in Fig. 5(d) with the variations of I_{FP}. Theoretically, the damping factor is related to the resonance frequency by $\gamma = \gamma_0 + K f_R^2$ [23,24], and we obtain the K-factor of 0.28 ns by linearly fitting γ versus f_R^2 as solid lines. The corresponding intrinsic ultimate damping limited 3 dB modulation bandwidth is evaluated to be 32 GHz when injecting a modulation signal into the FP as $I_{SQ} = 10$ mA based on the relation of $f_{3\,\text{dB,max}} = 2\sqrt{2}\pi/K$ [25], which is potentially achievable with improved cooling methods.

3. RELATIVE INTENSITY NOISE CHARACTERISTICS

The relative intensity noise is measured for the HSRL using the experimental setup shown in Fig. 6, under constant direct
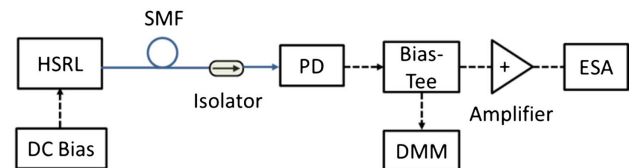

Fig. 6. Experimental setup for measuring the relative intensity noise characteristics for the HSRL. SMF, single-mode fiber; PD, photodetector; DMM, digital multimeter; ESA, electrical spectrum analyzer.

current biasing without microwave modulation input. The laser output is collimated into a tapered SMF and then passes through an optical isolator, followed by being fed into a high-speed photodetector (PD). The optical coupling efficiency to the fiber is estimated to be 50%. A 26.5 GHz bandwidth bias-Tee is then used to split the converted electrical signal into direct current (DC) and alternating current (AC) components, in which the DC signal indicates the detected photocurrent I_{dc} monitored by a digital multimeter, and the AC signal is amplified by two cascaded RF amplifiers each with 20 GHz bandwidth and 20 dB power gain. A 50 GHz bandwidth electrical spectrum analyzer (ESA) is used to measure the amplified microwave signal N_{RF}, which is regarded as the total noise term, including the laser RIN, thermal noise N_{th}, and shot noise of photodetector N_{shot}. Considering that the system thermal noise N_{th} is independent of the optical power, we can measure it by running the setup with the HSRL turned off while keeping the operation of the photodetector and amplifiers. Therefore, the intrinsic laser RIN can be determined by subtracting the thermal noise and photodetector shot noise from the total noise term [26]:

$$\text{RIN}(f) = \frac{[N_{RF}(f) - N_{th}(f)]/G(f) - N_{shot}}{P_{elec}}, \quad \textbf{(1)}$$

where $N_{shot} = 2qrP_0R_L = 2qI_{dc}R_L$ is the photodetector shot noise power spectral density, which rises proportionally to the detected input power P_0, i.e., the power coupled into SMF, and the responsivity r of the photodetector, q is the elementary charge, R_L is the load resistance, $G(f)$ is the total amplifier power gain, and $P_{elec} = I_{dc}^2R_L$ is the average output electrical power of the photodetector under P_0.

The laser RIN spectra are shown in Fig. 7 at different injection currents, for the HSRL. The RIN values decrease quickly with the increase of bias currents, especially with the rising of I_{FP} due to the distinct increase of laser output power and suppression of relaxation oscillation peaks, as shown in Figs. 2(a) and 5(a). In Fig. 7(b), slightly lower RIN is observed when increasing I_{SQ} from 5 to 15 mA, which is attributed to the relatively small increase in the photon density. At high bias currents of $I_{FP} = 45$ mA and $I_{SQ} = 15$ mA, the laser RIN nearly approaches the standard shot noise limit [24] $2h\nu/P =$ −164 dB/Hz corresponding to an output power of 6.5 mW, where P is the total optical output power from the HRSL. The RIN spectra show well-defined peaks at the relaxation oscillation frequency, which corresponds to the resonance peak frequency in small signal modulation response curves, as shown in Figs. 5(a) and 5(b), which confirms the correspondence between small signal modulation curves and RIN spectra. In addition, mode partition noises at the low frequency portion, which mainly come from the mode competition and coupling inside the laser cavity, have been greatly improved due to the high SMSR of the designed HSRL [12,13].

The RIN spectra are further fitted based on the formula characterized from rate equation with Langevin noise sources, as given in Refs. [24,27]:

$$\text{RIN}(f) = 16\pi(\Delta\nu)_{ST}\frac{1/(2\pi\tau_{\Delta N})^2 + f^2}{4\pi^2(f_R^2 - f^2)^2 + f^2\gamma^2} + \frac{2h\nu}{P}, \quad \textbf{(2)}$$
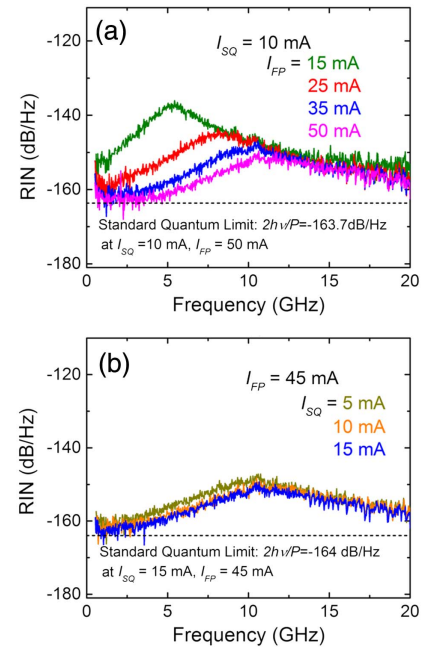

Fig. 7. Measured laser RIN with the variation of (a) I_{FP} as $I_{SQ} =$ 10 mA and (b) I_{SQ} as $I_{FP} = 45$ mA, respectively, for the HSRL with $a = 15$ μm, $d = 2$ μm, and $L = 300$ μm.

where f_R is the resonance frequency, γ is the damping factor, $(\Delta\nu)_{ST}$ is the modified Schawlow–Townes linewidth, $\tau_{\Delta N}$ is the differential carrier lifetime, h is the Planck constant, and ν is the optical frequency. The second term in Eq. (2) is the standard quantum noise limit indicating the minimum laser RIN under certain optical power P. Fitting the RIN curves in Figs. 7(a) and 7(b) by Eq. (2), we can obtain four basic parameters: f_R, γ, $(\Delta\nu)_{ST}$, $\tau_{\Delta N}$. The resonance frequency f_R and damping factor γ are extracted and plotted in Fig. 8, for the HSRL with the variation of I_{FP} as $I_{SQ} = 10$ mA. As shown in Fig. 8(a), the resonance frequencies f_R are plotted versus $(I_{FP} - I_{th})^{1/2}$ with the linear fitting slope D-factor of 2.07 GHz/mA$^{1/2}$ [23,24]. The resonance frequency saturates at high bias current due to laser thermal effect. Moreover, the damping factor γ as a function of the square of resonance frequency f_R^2 is shown in Fig. 8(b) with the variations of I_{FP} while I_{SQ} is kept constant at 10 mA. We obtain the K-factor of 0.25 ns by linearly fitting γ versus f_R^2 as solid lines.
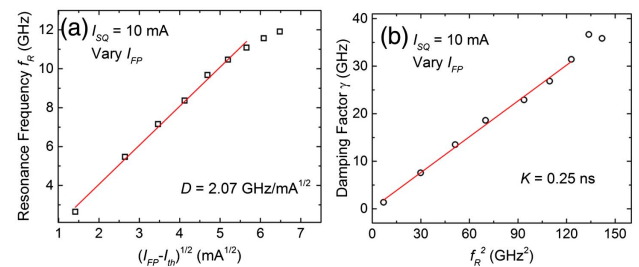

Fig. 8. (a) Resonance frequency versus square root of the injection current above threshold and (b) damping factor versus f_R^2 with variation of I_{FP} at $I_{SQ} = 10$ mA extracted from RIN measurements.

The intrinsic ultimate damping limited 3 dB modulation bandwidth is evaluated to be 36 GHz when small signal modulation is injected into the FP section as $I_{SQ} = 10$ mA. The damping factor extracted from the RIN curve is a little bit lower compared with the value obtained by small signal modulation curves, as shown in Fig. 5(d), which is due to the elimination of the parasitic parameters effect. Furthermore, the extracted modified Schawlow–Townes linewidths $(\Delta\nu)_{ST}$, which represent the laser field spectral purity considering only the spontaneous emission noise [28], are estimated to be 0.016–0.27 MHz, which is narrower than the measured value of 15 MHz, as shown in Fig. 4, due to influence of the carrier fluctuation noise and the circuitry [29]. With further improvements to the thermal effect and circuitry, perfect performances of stable single-mode operation HSRL with high speed and low noise can be realized.

4. CONCLUSION

In conclusion, we have investigated the modulation speed and noise characteristics of an HRSL, which is composed of an FP cavity with one of the reflection facets replaced by a square-shaped microcavity. High performance of a stable single-mode laser is obtained with SMSR over 40 dB over a large variation range of the injection current due to the strong mode selection of the square microcavity. And 3 dB bandwidth of 15.5 GHz is realized. As a consequence of reduced mode competition and lower carrier population fluctuation caused by the improvement of the SMSR, the HSRL microlaser exhibits excellent noise properties with the laser RIN reaching the standard quantum shot noise limit of −164 dB/Hz at high bias current with $I_{SQ} = 15$ mA and $I_{FP} = 45$ mA. With simple fabrication process and comparatively low cost, the HRSL with perfect characteristics such as stable single-mode operation, high speed, and low RIN noise is capable of functioning as a potential light source in high-speed optical fiber communications.

REFERENCES

1. A. B. Matsko and V. S. Ilchenko, "Optical resonators with whispering gallery modes I: basics," IEEE J. Sel. Top. Quantum Electron. **12**, 3–14 (2006).
2. A. W. Fang, H. Park, O. Cohen, R. Jones, M. J. Paniccia, and J. E. Bowers, "Electrically pumped hybrid AlGaInAs-silicon evanescent laser," Opt. Express **14**, 9203–9210 (2006).
3. J. Van Campenhout, P. Rojo-Romeo, P. Regreny, C. Seassal, D. Van Thourhout, S. Verstuyft, L. Di Cioccio, J. M. Fedeli, C. Lagahe, and R. Baets, "Electrically pumped InP-based microdisk lasers integrated with a nanophotonic silicon-on-insulator waveguide circuit," Opt. Express **15**, 6744–6749 (2007).
4. J. Ward and O. Benson, "WGM microresonators: sensing, lasing and fundamental optics with microspheres," Laser Photon. Rev. **5**, 553–570 (2011).
5. S. Yang, Y. Wang, and H. Sun, "Advances and prospects for whispering gallery mode microcavities," Adv. Opt. Mater. **3**, 1136–1162 (2015).
6. X. M. Lv, Y. Z. Huang, L. X. Zou, H. Long, and Y. Du, "Optimization of direct modulation rate for circular microlasers by adjusting mode Q factor," Laser Photon. Rev. **7**, 818–829 (2013).
7. L. X. Zou, Y. Z. Huang, X. M. Lv, H. Long, J. L. Xiao, Y. D. Yang, and Y. Du, "Dynamic characteristics of AlGaInAs/InP octagonal resonator microlaser," Appl. Phys. B **117**, 453–458 (2014).
8. N. H. Zhu, W. Li, J. M. Wen, W. Han, W. Chen, and L. Xie, "Enhanced modulation bandwidth of a Fabry-Pérot semiconductor laser subject to light injection from another Fabry-Pérot laser," IEEE J. Quantum Electron. **44**, 528–535 (2008).
9. H. Dalir and F. Koyama, "Bandwidth enhancement of single-mode VCSEL with lateral optical feedback of slow light," IEICE Electron. Express **8**, 1075–1081 (2011).
10. Z. X. Xiao, Y. Z. Huang, Y. D. Yang, M. Tang, and J. L. Xiao, "Modulation bandwidth enhancement for coupled twin-square micro-cavity lasers," Opt. Lett. **42**, 3173–3176 (2017).
11. S. I. Gonda and S. Mukai, "Degradation and intensity fluctuations in CW AlGaAs double-heterostructure junction lasers," IEEE J. Quantum Electron. **11**, 545–550 (1975).
12. G. P. Agrawal, "Mode-partition noise and intensity correlation in a two-mode semiconductor laser," Phys. Rev. A **37**, 2488–2494 (1988).
13. C. Su, J. Schlafer, and R. Lauer, "Explanation of low-frequency relative intensity noise in semiconductor lasers," Appl. Phys. Lett. **57**, 849–851 (1990).
14. H. X. Shi, D. Cohen, J. Barton, M. Majewski, L. A. Coldren, M. C. Larson, and G. A. Fish, "Relative intensity noise measurements of a widely tunable sampled-grating DBR laser," IEEE Photon. Technol. Lett. **14**, 759–761 (2002).
15. F. Tan, M. K. Wu, M. Liu, M. Feng, and N. Holonyak, "Relative intensity noise in high speed microcavity laser," Appl. Phys. Lett. **103**, 141116 (2013).
16. F. Tan, M. K. Wu, M. Liu, M. Feng, and N. Holonyak, "850 nm oxide-VCSEL with low relative intensity noise and 40 Gb/s error free data transmission," IEEE Photon. Technol. Lett. **26**, 289–292 (2014).
17. X. W. Ma, Y. Z. Huang, Y. D. Yang, J. L. Xiao, H. Z. Weng, and Z. X. Xiao, "Mode coupling in hybrid square-rectangular lasers for single mode operation," Appl. Phys. Lett. **109**, 071102 (2016).
18. X. W. Ma, Y. Z. Huang, Y. D. Yang, H. Z. Weng, J. L. Xiao, M. Tang, and Y. Du, "Mode and lasing characteristics for hybrid square-rectangular lasers," IEEE J. Sel. Top. Quantum Electron. **23**, 1500409 (2017).
19. H. Z. Weng, Y. Z. Huang, X. W. Ma, F. L. Wang, M. L. Liao, Y. D. Yang, and J. L. Xiao, "Spectral linewidth analysis for square microlasers," IEEE Photon. Technol. Lett. **29**, 1931–1934 (2017).
20. G. Morthier, R. Schatz, and O. Kjebon, "Extended modulation bandwidth of DBR and external cavity lasers by utilizing a cavity resonance for equalization," IEEE J. Quantum Electron. **36**, 1468–1475 (2000).
21. P. Bardella and I. Montrosset, "A new design procedure for DBR lasers exploiting the photon-photon resonance to achieve extended modulation bandwidth," IEEE J. Sel. Top. Quantum Electron. **19**, 1502408 (2013).
22. H. Dalir and F. Koyama, "High-speed operation of bow-tie-shaped oxide aperture VCSELs with photon-photon resonance," Appl. Phys. Express **7**, 022102 (2014).
23. P. Westbergh, J. S. Gustavsson, B. Kögel, Å. Haglund, and A. Larsson, "Impact of photon lifetime on high-speed VCSEL performance," IEEE J. Sel. Top. Quantum Electron. **17**, 1603–1613 (2011).
24. L. A. Coldren, S. W. Corzine, and M. L. Mashanovitch, *Diode Lasers and Photonic Integrated Circuits* (Wiley, 2012), p. 230.
25. R. Olshansky, P. Hill, V. Lanzisera, and W. Powazinik, "Frequency response of 1.3 μm InGaAsP high speed semiconductor lasers," IEEE J. Quantum Electron. **23**, 1410–1418 (1987).
26. F. Tan, R. Bambery, M. Feng, and N. Holonyak, Jr., "Relative intensity noise of a quantum well transistor laser," Appl. Phys. Lett. **101**, 151118 (2012).
27. Y. Yamamoto and N. Imoto, "Internal and external field fluctuations of a laser oscillator: Part I—Quantum mechanical Langevin treatment," IEEE J. Quantum Electron. **22**, 2032–2042 (1986).
28. C. Henry, "Theory of the linewidth of semiconductor lasers," IEEE J. Quantum Electron. **18**, 259–264 (1982).
29. L. Coldren, Y. Jan, T. Mason, M. Heimbuch, and S. Denbaars, "Properties of widely-tunable integrated WDM sources and receivers," in *10th IEEE Lasers and Electro-Optics Society Annual Meeting (LEOS)*, San Francisco, California, 1997, pp. 331–332.